

Chapter 1

Microscope Design for Simultaneous Measurements on Plasmonic Tips

AFM tips are characterised in a microscope custom-built for optical spectroscopy with simultaneous force and electronic measurements. The microscope is fully automated¹ and capable of running an assortment of experiments, the majority of which have been developed primary to study the optical response of tips. The primary experiment is designed to take two opposing AFM probe tips, align them in a tip-to-tip dimer geometry and demonstrate nm-scale precision motion/position control. Using such a setup, the plasmonic behaviour of both individual and coupled tip systems can be investigated. Using AuNP-tipped AFM tips in this system enables the dynamic study of the prototypical AuNP dimer under various conditions. Significant effort was invested into developing a system with the capability to perform these experiments. In this chapter the principles behind it's operation and the design considerations are discussed in depth.

1.1 Mechanical Design

To measure the physical properties of nanostructures on the sub-nm scale in ambient conditions is a difficult challenge. For a microscope to be capable of such measurements requires many careful considerations, the result of which is a compact experimental platform resistant to both vibrations and thermal effects.

The most important parts of any microscope are the sample stage and objective lens. For stable optical measurements these have to be locked together (**mechanically referenced**) in a symmetric configuration to prevent drift, mechanical or thermal, between the sample and the focal spot. An inverted microscope design provides the best stability and the microscope platform (Figure 1.1) is designed based on this concept. Mechanical drift is prevented by maintaining a close reference point between the sample and the objective. In this case the sample stage is pocketed into a top plate from which the objective is screwed so that any

¹A custom Python application used to control the microscope and all experiments

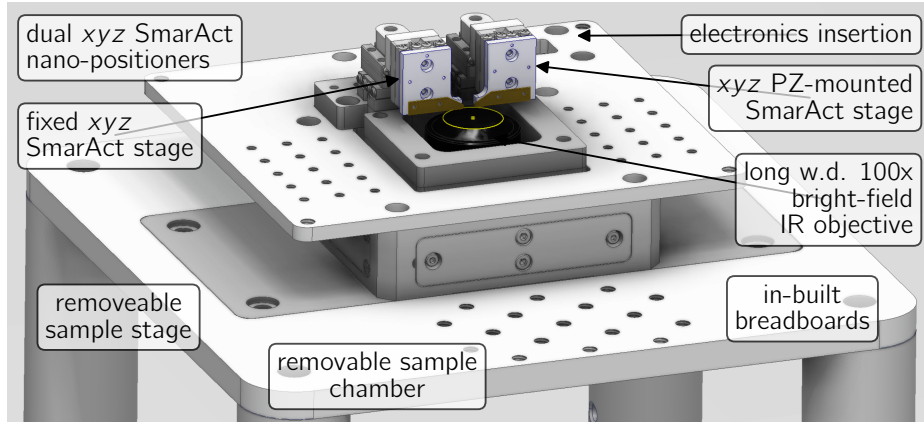
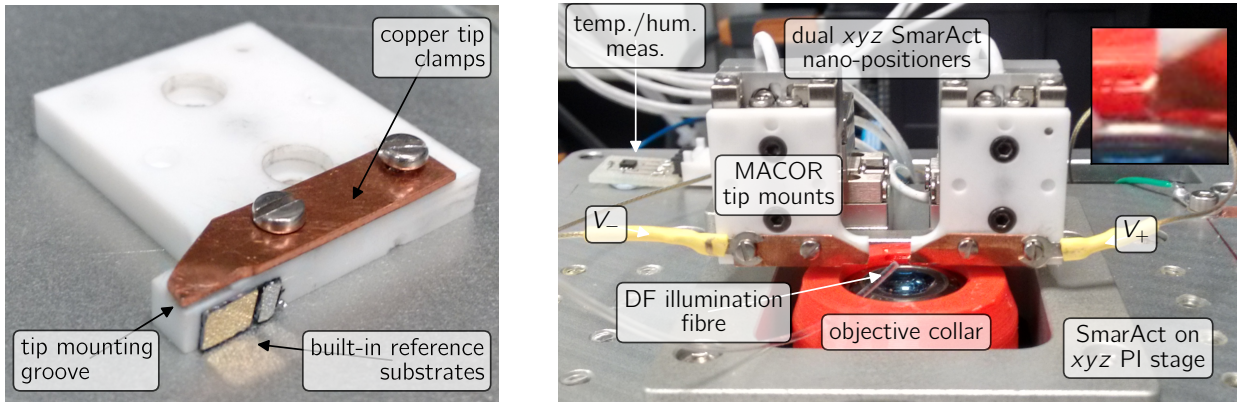


Figure 1.1: Mechanical design of the microscope. The main features of the inverted microscopy platform are highlighted, including two independent nanopositioners, one with piezo control, situated on a removable breadboard plate above the focus of an objective. Breadboard holes enable the mounting of optomechanics close to the sample. The top plate features a sealed lid with gas inlets for environmental control.

vibrations between sample and objective occur in phase. Thermal drift is prevented by exploiting symmetry such that any expansion is around the objective and that all mechanical plates expand at the same rate. Cast aluminium is also used for plate construction for its lower coefficient of thermal expansion compared to aluminium, whilst still remaining cheap and easily machinable compared with steel or titanium. The overall microscope platform is constructed 200 mm off the table on 1.5" diameter steel posts. The 200 mm height maintains stability without the need for cross-linking and is spacious enough to accommodate underside optics. The microscope platform and all important optics are mounted onto an anti-vibration stage to further reduce vibrations. All optics are mounted in either cage or lens tube, held 5 mm off the table and locked together.

The typical experiment sample setup is shown in Figure 1.2b. Samples are mounted onto either of two 3-axis slip-stick translation stages with 12 mm of travel and fine piezo control (SmarAct GmbH, SLC-1720-S w/ MCS), of which one is mounted onto a 3-axis piezo translation stage (PI GmbH, PI-733.3CD) for finer motion control. The top platform design is modular and easily removable, with alignment socket precise enough to relocate a sample to within 10 μm after removal. Multiple adapters are used to mount different samples onto the stage. A cover slip holder is used for nanoparticle characterisation while AFM chip holders (Figure 1.2a) are designed to mount tips. AFM probe mounts are made from machinable glass-ceramic (MACOR, Corning inc.) in order to prevent thermal expansion (coefficient of thermal expansion $\alpha_T = 9.3 \times 10^{-6} \text{ K}^{-1}$, compared to $\alpha_{T,\text{aluminium}} = 23.1 \times 10^{-6} \text{ K}^{-1}$ and $\alpha_{T,\text{titanium}} = 8.6 \times 10^{-6} \text{ K}^{-1}$ [1]) and to electrically insulate the mounts from the nanopositioners. The copper clamps holding the AFM probes are contacted to enable sample biasing with an applied voltage and to measure the current between two tips. Optical reference substrates



(a) Design of the tip mounts. Tips are placed in a rectangular groove in the insulating MACOR plate and held in place by an angled Cu clamp. Electrode solder tags are screwed down onto the clamp to electrically contact the tip. Mirror substrates are stuck onto the bottom of the mount to provide an easily accessible spectral referencing point.

(b) Design of the dual tip mount stage and dark-field illumination mechanics. Each nanopositioner with tip mount clamp is connected to an external electronic circuit. A 3D-printed, plastic collar is attached to the objective, holding a 1 mm diameter optical fibre for dark-field side-illumination of tips. A temperature and humidity sensor is attached to the back of the plate for environmental monitoring when the chamber is sealed.

Figure 1.2: Design of the dual tip microscope stage.

(0.3 mm Au- and Pt-coated AFM chips) for measuring the spectral content of the illumination are attached underneath the piezo-mounted stage for *in-situ* referencing.

The experimental chamber is sealed to control the gas environment (switchable between air bubbled through water and nitrogen to control humidity) and acts as a Faraday cage to reduce EMI incident on the sample. The chamber is equipped with a low pressure one-way valve and a needle valve to control the gas flow. Silencers are attached to the gas inlets with a foam surround to prevent air currents. The presence of a sealed chamber is enough to stabilise the sample against external air currents and helps to maintain a constant thermal equilibrium around the sample. A low magnification simple microscope, constructed from a disassembled webcam CCD, is attached to the roof of the chamber to aid the alignment of samples to the objective focus. Metal contacts connect the roof to the grounded base, transforming the chamber into a EMI-shielded Faraday cage. Optical windows on the sides of the chamber are used to insert secondary lasers perpendicular to the objective axis, used primarily with the AFM module. They also allow for external monitoring of the stage positions from the side.

1.2 Optical Design

The optical design employs the concept of reimaging spatial filters into the correct planes for efficient spectroscopy leading to a compact design. Employing reimaging means that beams

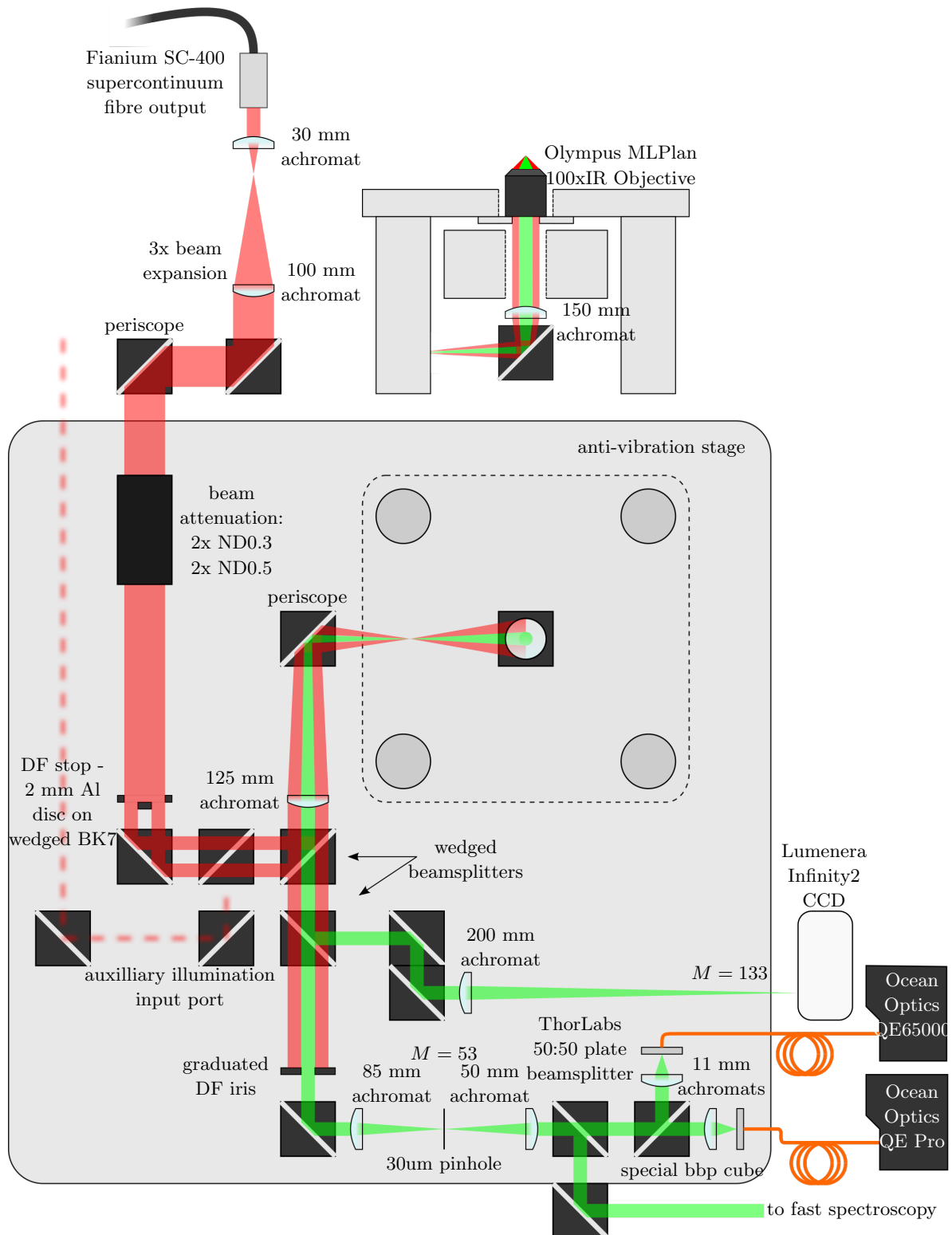


Figure 1.3: Diagram of the full optical layout and specification of the microscope.
All optics are accounted for except for silver periscope mirrors, which transfer the beam between platforms of differing height.

are not required to propagate exactly along the optical axis, minimising the number of long, empty beam lines, typically used for alignment. By reimaging the front and back focal planes of the objective, spatial and Fourier k -space filters are placed in the corresponding planes, ensuring optimum filtering performance and minimal aberration. A detailed schematic of the microscope platform and the surrounding optical bench layout, containing the specifications of all optics used, is found in Figure 1.3.

Both image and Fourier planes are set through careful placement of each set of lenses. The required minimum degrees of freedom for beam alignment are accounted for by mirrors placed in the focal and Fourier planes. Those in the Fourier planes change the position of the beam without affecting the beam shape, whereas those placed in the focal planes only change the beam shape since the k -space distribution is changed by the angular deviation. The position and shape of the beam are therefore independently adjustable, greatly simplifying beam alignment. This advantageous technique results in high beam quality, and as a direct result of the lack of long, iris-containing beam lines, results in a compact microscope.

A long working distance objective is required for imaging and spectroscopy. A bright-field (BF) long working distance IR objective (Olympus LMPlan 100 \times IR, 0.8 NA) is used to access wavelengths above 700 nm, for which the more convenient dark-field (DF) VIS objectives (Olympus LMPlan 100 \times BD) exhibit a sharp cutoff. A dark-field illumination/collection configuration is necessary for spectrally studying scattered light from a nanostructure. Dark-field refers to the use of high-angle ($NA = n \sin \theta \geq 0.7$) illumination, the reflections of which are filtered to collect only low-angle scattering from the focal plane. A large numerical aperture (NA) is required to properly study nanostructures in dark-field as it means light is collected across a large acceptance angle with a small focal length and large magnification. Since dark-field illumination is not supported on BF IR objectives light needs to be brought in externally in a side-illumination geometry. A 3d-printed objective collar is used to hold a 1 mm diameter optical fibre \sim 1–2 mm from the sample, outside of the objective collection angle, to which a cold white LED is fibre coupled. The fibre is fed through a breadboard hole in the top plate and sealed so as to preserve the environmental chamber integrity. The fibre outputs a broad cone of light which illuminates samples over a large area.

Use of a ultra-high brightness supercontinuum laser source (Fianium SC-400, 4 W, 480–1750 nm) enables single nanostructure spectroscopy with exposure times on $\mathcal{O}(10\text{ ms})$. The beam is expanded to fill the back aperture of the objective and apertured into a ring to mimic dark-field illumination using a dark-field disc stop. The inner diameter of the ring is set at 2 mm and the outer diameter is set by the back aperture of the objective, in this case 3 mm. Reflective neutral density filters totalling ND1.6 (2.5% transmission) are placed in the beam line to reduce the incident power on the sample. The majority of the initial incident power is lost on the dark-field stop. Further attenuation results from the 10:90 (R:T) beamsplitter used

to relay the laser into the microscope. At this point the power is reduced to 1 mW, as measured on a bolometer (Coherent) behind the objective, to prevent laser damage to samples. Whilst the power is seemingly low and comparable with high-brightness incoherent light sources, the focussing ability of the single mode laser results in an intense, diffraction-limited, white light focus not possible with incoherent sources. Assuming a spot size on $\mathcal{O}(1 \mu\text{m})$ the focal intensity is on $\mathcal{O}(10^8 \text{ mW/cm}^2)$.

The incident light is apertured and reimaged directly onto the back focal (Fourier) plane of the objective, as opposed to aperturing close to the objective back aperture, to prevent diffractive artefacts in the conjugate plane of the collected light. The ring aperture means that the focus is illuminated only at high-NA as with conventional dark-field spectroscopy. Scattered light is then filtered by the dark-field iris in the return beam path to collect only low-NA scattering, removing any signal contribution from reflected illumination. Reimaging allows both the dark-field iris and stop to be located away from the objective for convenient access and easy adjustment. Alternative designs using optics mounted at the objective back aperture do not benefit from having the stop and iris in conjugate planes and may require motorised irises if not accessible by hand. For this experiment a simple graduated dark-field iris is sufficient for external use to filter the collected light signal.

Since incident power is not an issue, and in many cases requires significant attenuation, the microscope is optimised for efficient collection. The 10:90 beamsplitter used for laser input means only 10% of collected light is lost when returning back through the main microscope arm. Furthermore, all optics in the system are optimised for light between 500–1100 nm.² The angle-dependent Fresnel coefficients of the glass used in all optics components mean that *p*-polarised light is favoured during transmission.³ A 90° turning periscope is placed after the first reimaging lens to reverse the initial linear polarisations of light so that the axial polarisation with respect to the tip axis has highest transmission through the beamsplitters in the collection path.

Subsequently, collected light is split into imaging and spectroscopy paths using a second (50:50) beamsplitter placed before the dark-field iris. CCD imaging is both used to align and characterise the laser focus and to centre samples onto the targeted laser illumination spot. Sample imaging uses light collected from the scattered side-illumination white LED light to produce dark-field images whereas the laser light is not DF-filtered in this path. Images are magnified 133×. Light passing along the spectroscopy path is filtered to remove any contributions from reflected light to the scattering signal. A graduated iris is used to remove the 2 mm outer-ring (high-NA components) of the returning beam. The iris is placed

²Achieved via exclusive use of Ag mirrors, Edmund Optics VIS-NIR AR coating on lenses, COMAR NIR and ThorLabs visible or visible-NIR coatings on beamsplitters

³All beamsplitters have some degree of polarisation sensitivity due to Fresnel coefficients of the glass used. Reflectance can be a factor of 2 different between orthogonal linear polarisations. For comparison of glass reflectances and Fresnel coefficients

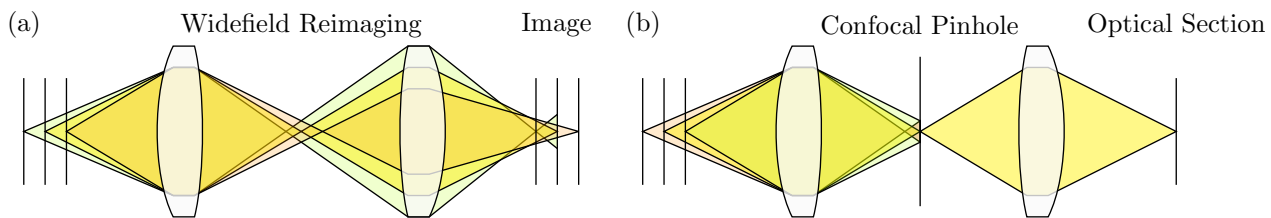


Figure 1.4: Diagram of optical sectioning in confocal microscopy. (a) Out of focus light from nearby reimaged focal planes leads to blur and a decrease of resolution in images. (b) Images spatially filtered in the focal plane by a confocal pinhole localise light from only a select volume that is sufficiently focussed to pass through the pinhole aperture.

in the image plane of the dark-field stop (Fourier plane) for the most accurate filtering and **optimal/optimum** performance. The two beamsplitters present before the dark-field iris are wedged to prevent ghost images, which transmit through the closed iris and create spectral artefacts. However, the 5 mm thickness of wedged beamsplitters means increased dispersion and the limited availability of broadband AR coatings results in reduced reflectance in the NIR. Additionally, the DF-filtering process only works to remove light reflected out at the same angle. Angled samples (such as the facets of tips) can reflect light into the low-NA collection, creating more spectral artefacts. It is for this reason that the flat tip facets are even visible in a dark-field configuration.

Since the laser focusses to a diffraction-limited spot on the sample, spectra are collected from a small sampling volume. Further spectral localisation is achieved by confocally filtering the image plane after the iris using a 30 μm pinhole to collect light from only the central focal spot. Only light in focus on the pinhole may pass through it. By rejecting out of focus light the image becomes an optical section with a tight depth of focus. The size of the pinhole sets both the lateral and axial width of the transmitted in-focus light. The combination of spatial masking and optical sectioning creates a localised sampling volume in the objective-sample plane. This effect is shown in Figure 1.4. The location of the spatial mask image, demagnified 53 \times , in the objective focus, setting the sampling volume, is controlled by a mirror before the confocal filtering array. A slip-in disassembled webcam is used to image the Fourier plane before and after confocal filtering to measure the collection geometry.

Confocal filtering not only improves the contrast but also improves upon the wide-field, diffraction-limited resolution by up to a factor of $\sqrt{2}$ at the cost of image brightness []. This is a result of the removal of higher diffraction orders by the pinhole thereby increasing the resolution. A decrease in the Rayleigh criterion [] for diffraction-limited resolution, r_{lateral} , given by,

$$r_{\text{lateral}} = \frac{1.22\lambda}{(NA_{\text{obj}} + NA_{\text{cond}})} = \frac{0.61\lambda}{NA}, \quad (1.1)$$

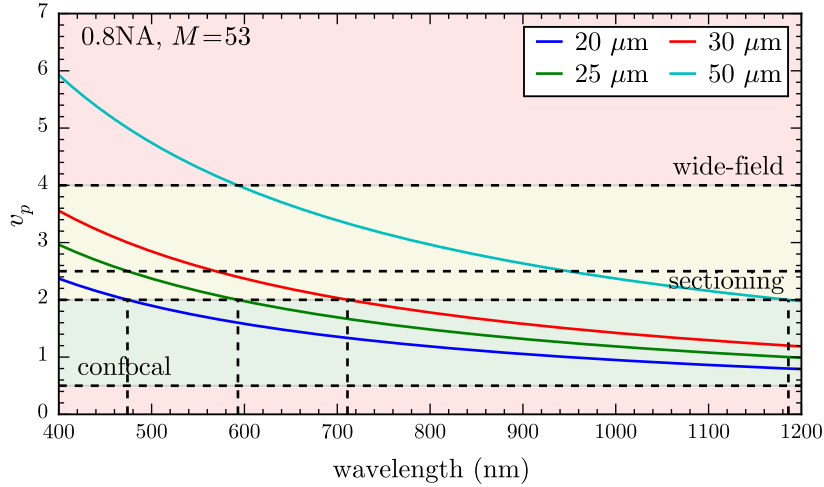


Figure 1.5: Optimum confocal pinhole size across the visible-NIR spectrum.

in expected in an epi-illumination geometry, to around,

$$r_{\text{lateral}} = \frac{0.37\lambda}{NA} \quad (1.2)$$

[]. The axial resolution, r_{axial} , is also improved to,

$$r_{\text{axial}} = \sqrt{\left(\frac{n\lambda}{NA^2}\right)^2 + \left(\frac{\sqrt{2}nd_p}{NA}\right)^2}. \quad (1.3)$$

Decreasing the pinhole diameter not only decreases the thickness of the optical section but the minimum resolvable lateral distance. Since the depth of focus scales as M^2 the placement of the pinhole along the beam path is not critical. Choice of pinhole diameter, however, is important.

Realistically, however the detector is not a point detector but a finite aperture, so the collection point spread function (PSF) must be convoluted with the detector rect function, D , giving an image PSF $I = |h_1|^2(|h_2|^2*D)$. The FWHM of the image intensity retains the $\sqrt{2}$ improvement if the detector width $v_p \leq 0.5$, but realistically this leads to a significant loss in brightness. Resolution is improved until $v_p \geq 4$, at which point the wide-field behaviour is recovered. Practically $v_p \leq 2$ to optimise lateral resolution and $v_p \leq 4$ to optimise depth resolution. The optimum pinhole diameter is calculated using,

$$\frac{M}{NA} \geq \frac{\pi d_p}{v_p \lambda}, \quad (1.4)$$

where d_p is the pinhole diameter. A sufficiently small pinhole diameter will have $v_p = 2$, therefore for a 0.8NA, $M = 53$ system $d_p/\lambda \leq 45$, e.g. 22 μm at 500 nm and 50 μm at

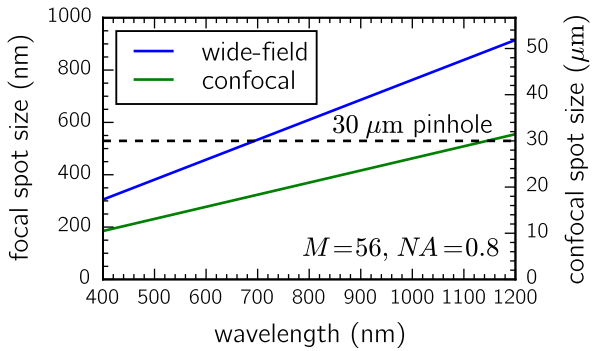


Figure 1.6: Magnified diffraction limited spot sizes for Gaussian beam focuses compared with the confocal pinhole diameter. Larger wavelengths have larger focusses, therefore wavelengths with spot sizes greater than the pinhole diameter begin to get cut. Increased spatial localisation results in decreased spectral bandwidth.

1100 nm.

Since the incident laser illumination is not also confocally filtered, as required for idealistic point excitation, and exhibits a non-Airy diffraction pattern, a significant increase in resolution to the confocal limit is not expected. Confocal spectroscopy is moreso used for the lateral spatial localisation when studying extended nanostructures.

One limitation to the confocal technique is the choice of pinhole diameter. It is usual in confocal imaging to select a pinhole in terms of Airy units (A.u.). The width of the central maxima of the focus profile is defined as 1 A.u., to which the pinhole should be optimally between 0.5 and 1 A.u.. The value of an Airy unit is wavelength dependent as it depends on the focus spot size, hence the pinhole will effect white light differently across the spectrum. It is assumed that the pinhole size is fixed at 1 A.u. at a specific threshold wavelength. At the chosen threshold wavelength the pinhole behaves as expected. For wavelengths shorter than the threshold $d > 1 \text{ A.u.}$, therefore the whole diffraction pattern transmits, giving little benefit of confocal localisation. For wavelengths much larger than the threshold $d < 0.5 \text{ A.u.}$ and the throughput of light begins to decrease as the edges of the focus are cut. A drop in signal in the NIR is therefore expected.⁴ The pinhole parameters and focal spot sizes of an assumed Gaussian beam, taking account the magnification ($M = 56$) from the sample plane to the pinhole plane, are shown in Figure 1.6. Use of a 30 μm pinhole diameter was determined based on k -space images of beam structure (see below). The diameter sets 1 A.u. at 600 nm with cut-off beginning around 800 nm.

Once filtered only the spectral content of the beam is of interest rather than the image so strict adherence to conjugate planes is no longer necessary. The beam is split 50:50 into two signals, with one going to the benchtop spectrometers and the other to a fast spectroscopy path.⁵

⁴This is also the case when focussing into a fibre.

⁵The fast spectroscopy technique is developed and implemented but otherwise not used in any experiments

The benchtop spectroscopy signal is further split into linear s and p polarisation components using a broadband polarising beamsplitter cube (Melles-Griot 300–1100 nm). Broadband polarisers (Thorlabs 500–1500 nm) oriented along the s and p axes are placed at the cube output ports to increase the extinction. Each polarised signal component is then finally focussed into multi-mode fibres, using short focal length (11 mm) lenses to achieve a spot size smaller than the fibre core. 100 μm fibre core is used instead of 50 μm to reduce laser speckle in spectra since the 30 μm confocal pinhole diameter already localises the signal. The spectral signal from each of the fibres is recorded using TE-cooled, benchtop spectrometers (Ocean Optics QE65000 and QE Pro) with integration times on the order $\mathcal{O}(10 \text{ ms})$. The Si detectors in the spectrometers have a significant drop off in sensitivity beyond 900 nm, imposing a limit to detectable signals of around 1100 nm. The supercontinuum laser imposes a 480 nm spectral cut-on, resulting in an effective measurement window of 500–1100 nm.

Measured spectra are background-subtracted and referenced to the spectral density of the supercontinuum illumination as transmitted through the microscope optics. The high brightness of the supercontinuum laser with 10 ms exposures mean that the relative intensity contribution from external light sources is negligible. Background subtraction is therefore mostly required to remove the dark counts inherent on the CCD. The coherence of the supercontinuum laser means that conventional referencing using scatter from a white diffuser to map the illumination spectral density is not possible. Instead, reflections from a reflective substrate attached underneath the piezo-mounted sample mount are used as a reference. Different mirror substrates are used depending on the sample. For metallic samples the mirror substrate is matched to the metal so only structural spectral features are observed. Otherwise either a Ag mirror or glass slide are sufficient for referencing as they provide relatively flat reflectances across the visible-NIR spectrum. As optics are very rarely broadband between 400–1200 nm, all non-essential pathways are closed when acquiring spectra to prevent artefacts. Back reflections off lenses are found to superimpose a weak duplicate of the illumination spectrum onto spectra since the reflections are translated in k -space and are therefore not completely filtered by the dark-field iris.

1.2.1 Characterisation of Microscope Performance

During most experiments the power incident on samples is kept below 1 mW corresponding to a focal intensity of $\sim 10^8 \text{ mW cm}^{-2}$. This is used to maintain sufficient signal quality whilst preventing damage or destructive changes to nanoscale Au samples (typically 50 nm Au coatings). Beam profiling is used to characterise beam propagation in the microscope and determine its ability to collect dark-field spectra. Profiling is carried out using focal scans of both reflected light from a Ag mirror and scattered light from an 80 nm AuNP, measured simultaneously in the current project. For this reason it's operation is omitted from this work.

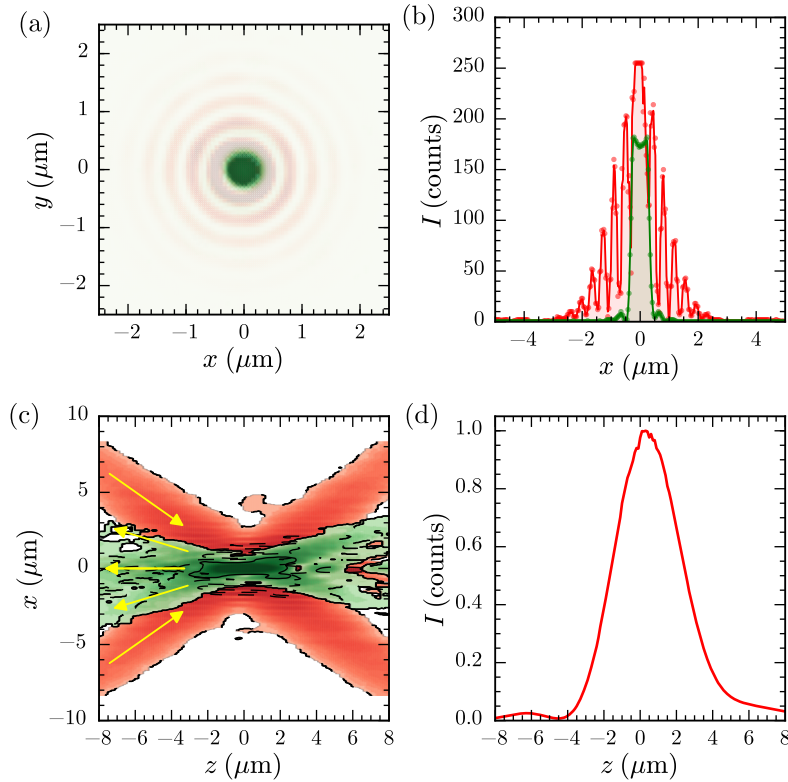


Figure 1.7: Beam profiling of dark-field filtered supercontinuum illumination (red) and scattering collection (green) beam lines. The spectroscopy pathway is characterised by coupling a 532 nm laser into a single mode fibre and through the collection optics with the DF-iris closed to 2 mm. Supercontinuum laser light is reflected back from a Ag mirror. The stated axial distance z is twice the displacement of the mirror to account for reflections to the focal plane. Lateral distances are calculated using the CCD array size and pixel dimensions. (a) Lateral beam profile of the illumination and collection focusses as measured on the CCD. (b) Intensity cross sections through the lateral beam profiles of the illumination and collection. (c) Axial cross section through the focus of illumination and collection beams. (d) Normalised summation of spectrometer counts of confocally localised supercontinuum light passing through the collection optics.

on a CCD and a spectrometer. The CCD is used to laterally profile the beam through the focus while the spectrometer characterises the confocal profile and spectral distribution of the light. Both the illumination and collection pathways are profiled. The illumination pathway is profiled using the dark-field filtered supercontinuum beam while one of the collection fibres is removed from its spectrometer and is coupled with a 532 nm single mode laser to profile the collection pathway.

Figure 1.7 shows both the lateral focal spot on the CCD and relevant cross sections along the optical and focal axes for both the illumination and collection optics, along with depth-profiling using broadband-integrated spectra. Figure 1.7a shows the beam structure in the focus. The single mode fibre output has a Gaussian beam profile focus while the ring aperture of the supercontinuum beam achieves a tighter focus but with more power concentrated in its outer rings (Figure 1.7b). The axial cross section of beams (Figure 1.7c) shows the focussing of

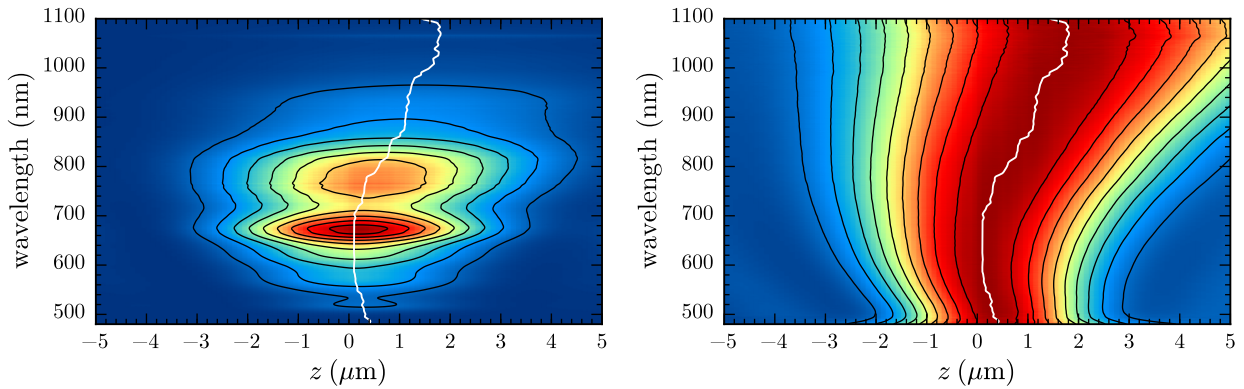


Figure 1.8: Axial chromatic aberration at each wavelength through the objective focus. The image is formed from spectra of the *s*-polarised component of a reflection from a Ag mirror scanned through the focus. An intensity plot normalised for each wavelength is shown to determine depth of focus. The white indicates the position of maximum signal along the optical axis for each wavelength and shows the distinctive bowing curve of chromatic aberration.

the high angle (0.71–0.8 NA, 45–53° incident angle) supercontinuum ring. The DF-iris restricts the collection angle of light from the focus to below ∼32°, depending on closure extent, to reject the high angle supercontinuum components. After confocally filtering the depth of focus of the sampling volume is 4 μm (Figure 1.7d). This could potentially be improved by confocally filtering the supercontinuum input to become similar to a true confocal microscopes. For most cases it is not necessary since samples are suspended nanostructures and depth profiling is not necessary.

Figure 1.8 shows the individual wavelength components that make up the integrated spectral signal in Figure 1.7d. As expected the depth of focus increases with wavelength. The depth varies from 2.5 μm at $\lambda = 500$ nm to 5.5 μm at $\lambda = 1100$ nm, **typical values for confocal microscopes at these wavelengths** [1]. The chromatic structure of the beam is non-linear and shows that the colour maxima for $\lambda < 550$ nm and $\lambda > 800$ nm occur slightly offset from the pinhole position. Overall this does not detract much from the measured spectra since intensity differences in the chosen focal plane are normalised with the reference.

Lateral localisation is more important to consider than axial sectioning. The true lateral resolution is difficult to characterise due to the large broadband focal spot and its ringed structure. Scattered light from a sub-wavelength size nanoparticle provides a point source for measuring the PSF across a small, resonant bandwidth. The measured lateral scattering response of a confocally (raster-) scanned 80 nm AuNP at its resonant frequency, $\lambda_{LSP} = 550$ nm, is shown in Figure 1.9. Images are acquired by raster-scanning over a grid containing a AuNP and measuring the spectrum at each pixel, from which a single wavelength slice is extracted. The confocal pinhole is replaced and the optics realigned between scans of the same AuNP. Without a pinhole the image of the AuNP is a convolution of the supercontinuum light focal pattern (Figure 1.7a) and the AuNP scattering point source. Its spectrum is a

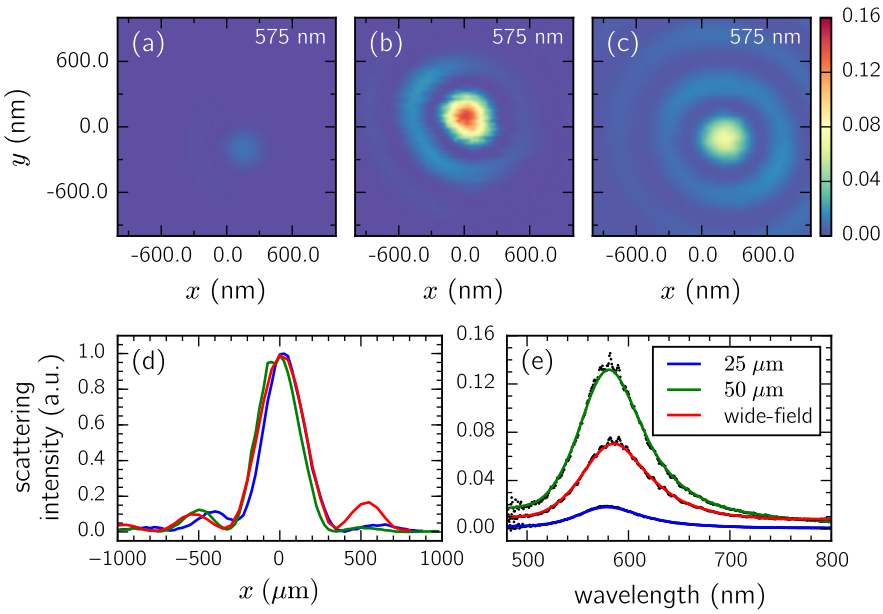


Figure 1.9: Hyperspectral scans of AuNPs used to characterise the lateral PSF with different confocal pinhole diameters. (a-c) Wavelength slices of AuNP scans on resonance using 25 μm and 50 μm diameter pinholes and finally no pinhole, respectively. (d) The extracted PSF from line profiles across the images (a-c). (e) Spectra of AuNPs imaged. Localisation is observed as the concentric illumination rings are cut as the pinhole diameter is reduced.

convolution of its own plasmon resonance and the supercontinuum spectrum at each point in the pattern. The spectrum is normalised against the laterally-integrated spectrum of the supercontinuum laser reflected off a Au mirror to only show the plasmon resonance. From the images (Figure 1.9a–c) it is clear that the addition of a pinhole restricts the spatial extent of the PSF by filtering the contribution of the outer illumination rings to the image. The pinhole diameter is reduced until only the central focus remains. Identifying this point becomes difficult as diffraction from the pinhole aperture blurs the focus in the focal planes after the pinhole. This occurs when using a 30 μm pinhole, and is primarily why that diameter pinhole was chosen. Larger pinholes (only 50 μm tested) let through a larger portion of the outer rings while there is no more gain in localisation from smaller pinholes (25 μm tested), instead losing only signal. The width of the central maximum in the PSF (Figure 1.9(d)) is also only marginally reduced between pinhole sizes so there is little gain in resolution.

Chromatic aberration in the scattering signal across the resonance bandwidth can also be determined from the hyperspectral image stacks. The central position of the scattering centroids are extracted from each of the wavelength slices in the hyperspectral image. Changes in the centroid position between wavelength images signifies chromatic aberration. The extent of chromatic aberration in the sample plane is shown in Figure 1.10. Characterising this aberration, if systematic, means that the lateral position of wavelength images in the hyperspectral stack can be adjusted to correct for chromatic aberration. This has its advantages

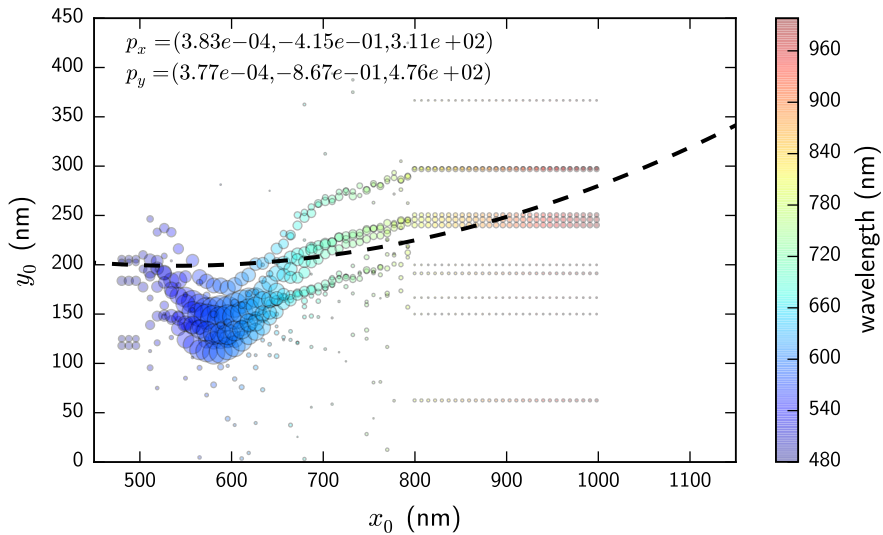


Figure 1.10: Measurements of lateral chromatic aberration across the plasmon resonance scattering bandwidth from hyperspectral images of AuNP. The central position of the scattering centroid is extracted from images at each wavelength. Changes in centroid position with wavelength signify chromatic aberration.

when recombining the individual wavelength images back into a colour image or colourmap.

To summarise, beam profiling clearly shows that the supercontinuum dark-field technique works as expected and that spectra are collected from a small volume in the objective focus. This is significantly improved by implementing confocal microscopy to spatially localise spectra.

1.3 Electronics Design

The experiment chamber contains two triaxial connectors to send and return electronic signals through the chamber. These are wired to the Cu tip clamps to permit measurements of the electrical signal from the gap between the tips of two AFM probes. Control of electronics is done using a signal routing box to which the chamber triax cables are attached. Electronics are split between the a.c. electronics that drive the resonant tip alignment procedure and the d.c. measurement electronics. The d.c. electronics are further split into a low and high bandwidth measurement circuit. The low bandwidth (< 10 Hz) circuit measures electronics continually over long time periods, typically giving spatial information linked to sample separation. The high bandwidth circuit operates on a trigger to capture single shot events on much shorter time scales. The d.c. circuits are typically ran simultaneously while the a.c. and d.c. circuits are manually switchable. The schematic of this system is shown in Figure 1.11.

The a.c. circuit consists of a simple signal generator connected to a $20\times$ voltage amplifier to drive the junction capacitance. This is used to resonantly drive an AFM cantilever into

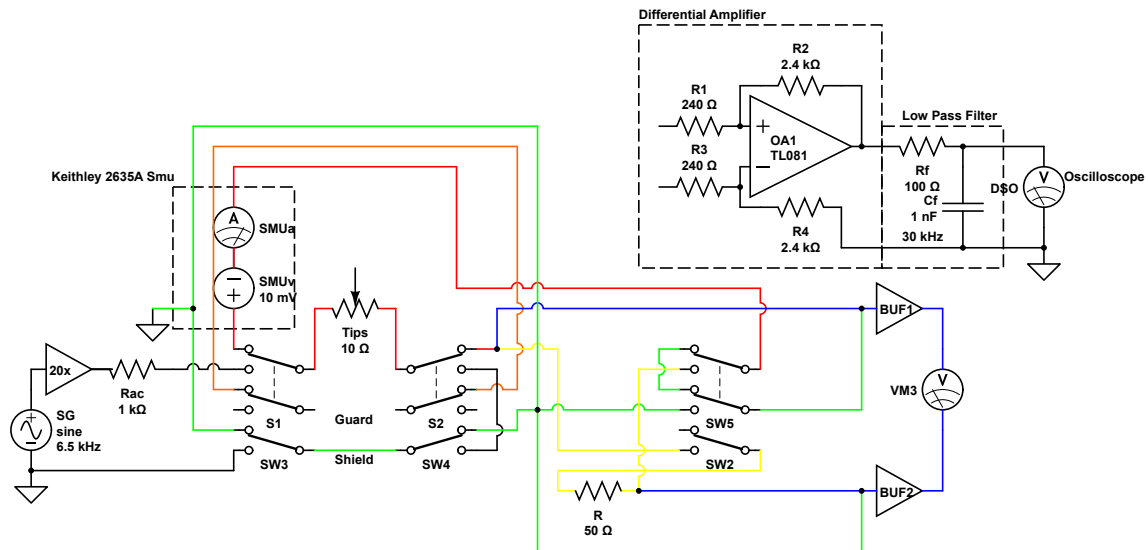


Figure 1.11: Schematic of the electrical measurement circuit. The central routing box allows switching between a.c. and d.c. circuits and low-and high-bandwidth d.c. measurements. The a.c. circuit is used to align two AFM probes together while the d.c. circuit is used to measure spatially dependent signals from the gap between two AFM probes.

oscillation and align tips into a tip-to-tip dimer configuration. A $200\ \Omega$ current limiting resistor is placed after the amplifier to prevent damage to the tip junction in the event of a direct conductive contact.⁶ The circuit is then terminated at ground. The separate d.c. circuit consists of a source-meter unit (SMU, Keithley 2635A) used to apply a voltage across the junction and measure the current through the junction. The switchable high-bandwidth path routes the current through a $10^4\times$ gain transimpedance amplifier (Femto DLPCA-200) and then a further combined $10\times$ amplification/1 MHz low-pass filtering stage (SRS SR560). The amplified voltage is measured on a digital storage oscillation (DSO) with the shield forming the return path for the current back to the SMU via the routing box.

The fundamental feature of combined circuitry is their separability. The a.c. circuit is not required to be low-noise but the d.c. circuitry is used to measure low-level currents. For the d.c. circuit to operate correctly it must be isolated from the other electronics. The a.c. circuit remains completely disconnected and grounded when the d.c. circuit is in operation. In such an experiment where the aim is to measure small, sensitive currents, reducing the noise to a minimum is imperative. The noise floor at low bandwidths sets the minimum current which can be measured while the noise at high bandwidth (high frequencies) sets the conductance resolution and minimum trigger level for single shot measurements. The reduced bandwidth of the SMU ($< 10\text{ Hz}$) removes much of the noise from basic measurements. Noise is reduced by using manual toggles switches over electrically controlled relays. All electronic chassis are grounded to a single point on the SMU to prevent EMI coupling and ground loops. Triax

⁶The optimum resistance value is calculated using $R = V/I_{\text{limit}}$ where $V = 15\text{ V}$ typically and a safe current limit is $I_{\text{limit}} = 500\ \mu\text{A}$. This gives a resistance of $30\ \text{k}\Omega$.

cabling is used with guarded connections running through the system except at the experiment chamber, which is grounded, to prevent leakage currents.

The operating standards and limitations of the high bandwidth measurement circuit are shown in Fig. 1.12. The value of the current limiting resistor, R , used to prevent overloading in the circuit is determined from these calculations using,

$$R = \frac{AV}{0.95V_{\text{overload}}}, \quad (1.5)$$

where V is the operating voltage of the measurement circuit, A is the amplifier gain and V_{overload} is the minimum overload voltage for the circuit at a given voltage V (determined by whichever limit is surpassed first, either the maximum input current of 5 mA pre-amplification or the maximum output voltage of 5 V)⁷. The prefactor of 0.95 is used to prevent the current getting to the actual overload point. As it is assumed that we aim to work at 10 mV (reasonable since we want good signal to noise with minimal electrostatic tip attraction and chance to overload the input/output current amplifier stages) a resistance of 240Ω is used as it is close to the calculated value and provides some extra headroom for increasing the voltage.

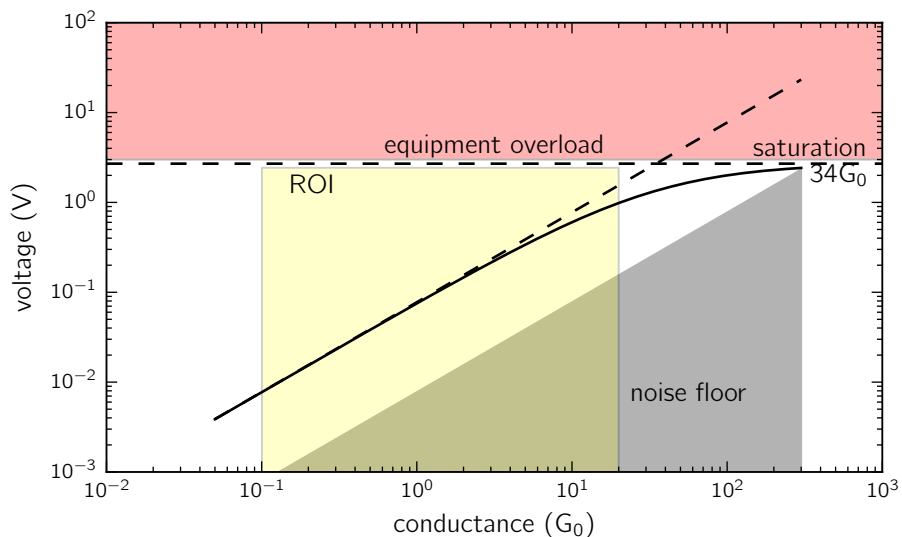


Figure 1.12: Characterisation of electronic measurements based on junction conductance. Solid lines show the calculated oscilloscope voltages for given junction conductances at selected voltages with use of current limiting resistor of $R = 241 \Omega$ to prevent saturation. Dashed lines show the calculated oscilloscope voltages for the case without the current limiting resistor.

The overload/saturation characteristics come from the data sheets of the SRS SR570 current amplifier while the noise floor is measured. The minimum trigger level is determined as the point at which the measured voltage crosses the noise floor, below which the noise will

⁷The relation between the current input into the amplifier and the amplifier output voltage is $V = AI$ hence $I_{\text{limit}} = V_{\text{overload}}/A$

incur false triggers.

Experimental Considerations For accurate electronic measurements using this circuit the series resistance is required to be measured to high precision. This is achieved using a SMU (Keithley 2635A).

Inverting this limiting resistance using $G = 1/R$ gives us a conductance limit to measurements. Conductances greater than this are small compared to the current limiting series resistance and are thus much harder to measure reliably. Ideally this value should be outside of the region of interest to prevent measurement error once the series resistance has been accounted for.

Current and transimpedance voltage measurements using the electronics circuit take the included series resistance into account using,

$$G_{\text{junction}} = (G_{\text{measured}}^{-1} - R_{\text{series}})^{-1}. \quad (1.6)$$

Characterisation of the Electronics Conductance measurements are validated by...

1.4 AFM Design: Measurements of Force

Force is measured using an atomic force microscopy (AFM) module to measure cantilever deflections as they flex under an applied force. The linear displacement of the cantilever, Δz , from its equilibrium position under an applied force, F , is given simply by,

$$F = k\Delta z, \quad (1.7)$$

where k is the stiffness or spring constant of the cantilever. Contact and tapping mode cantilevers are most used in experiments, for which $k = 0.2 \text{ N m}^{-1}$ and 40 N m^{-1} , respectively. The change in angle caused by a linear displacement at the tip can be measured optically as a change in deflection angle of a laser focussed on the back of a reflective cantilever. This sensitivity of this technique has led to it being named atomic force microscopy since atomic-scale forces cause measurable deflections enabling topological imaging with **atomic/sub-nm** resolution. For tip-tip systems nano-scale force measurements become important as they dictate how tips come together and move through interfacial layers prior to electrical contact. To this extent a com-

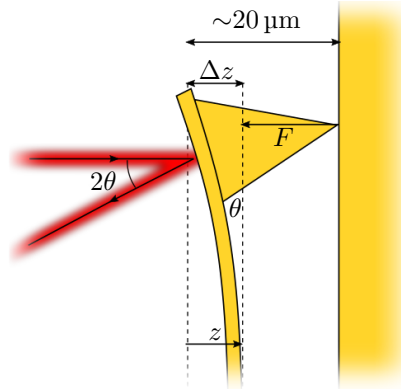


Figure 1.13: Concept of contact mode AFM. An applied force F bends the cantilever proportional to a linear displacement x . Light incident on the bent cantilever deflects at an angle 2θ .

pact AFM module was constructed to monitor the tip-tip interaction forces during tip dimer measurements/experiments/scans.

The AFM module consists of a compact optomechanical array mechanically bolted onto the top plate of the microscope platform and a separate 633 nm laser diode coupled together using strain-relieved single mode fibre. Single mode fibre is used to produce a stabilised laser output.⁸ Light is focused through an entry window in the experimental chamber onto the cantilever of the soft AFM probe in an experiment. The beam position is laterally offset on the focussing lens using a silver turning prism to focus on the cantilever at an angle so that reflections return through the AFM with the opposite lateral offset. An alternative to this approach allows use of a common beam path but requires two polarisers and a quarter wave plate, leading to simpler alignment but a more costly design. As the light is reflected back off the cantilever at a different angle in the focal plane it is laterally translated in Fourier space. This translation is measured using a fast lateral effect photodiode, also known as a position sensitive detector (PSD). The PSD contains a signal processing circuit with an in-built transimpedance amplifier to convert the small currents into voltages corresponding to the measurements $\Delta x, y$ and $\sum x, y$. Voltages are recorded using a DAQ card (NI X-series). A diagram of this arrangement is shown in Figure 1.14.

The width of the cantilevers used and the radius of the input beam determines the minimum beam size. The cantilevers have a width of 50 μm and therefore the spot size in the focus must be less than this value. Since the input is a single mode Gaussian beam the spot diameter, $2w_0$, can be calculated using,

$$2w_0 = \frac{4\lambda}{\pi} \frac{f}{D}, \quad (1.8)$$

where f is the focal length and D is the collimated beam diameter. For $\lambda = 633 \text{ nm}$ and a required spot size $2w_0 < 50 \mu\text{m}$ the fraction $f/D < 62$. The focal length is optimised first as there is a limit imposed by the distance from the edge of the top plate to the objective focus through the chamber window. For this reason a 100 mm lens is chosen, which restricts the beam diameter to $D > 1.6 \text{ mm}$. The beam diameter is set by the short focal length lens collimated the single mode fibre output and the iris afterwards.

Changes in the voltage output of the PSD are correlated with force applied to the tip at the end of the cantilever allowing the applied force to be measured. The position of the PSD is adjusted with zero force applied to an AFM cantilever so that zero voltage corresponds to zero applied force. The lateral displacement of the returning beam is then calculated using,

$$ds_{x,y} = \frac{\Delta V_{x,y}}{\sum V_{x,y}}, \quad (1.9)$$

⁸Stabilised output results from single mode operation. Multimode stability leads to significant intensity changes that cause issues with the lateral effect photodiode.

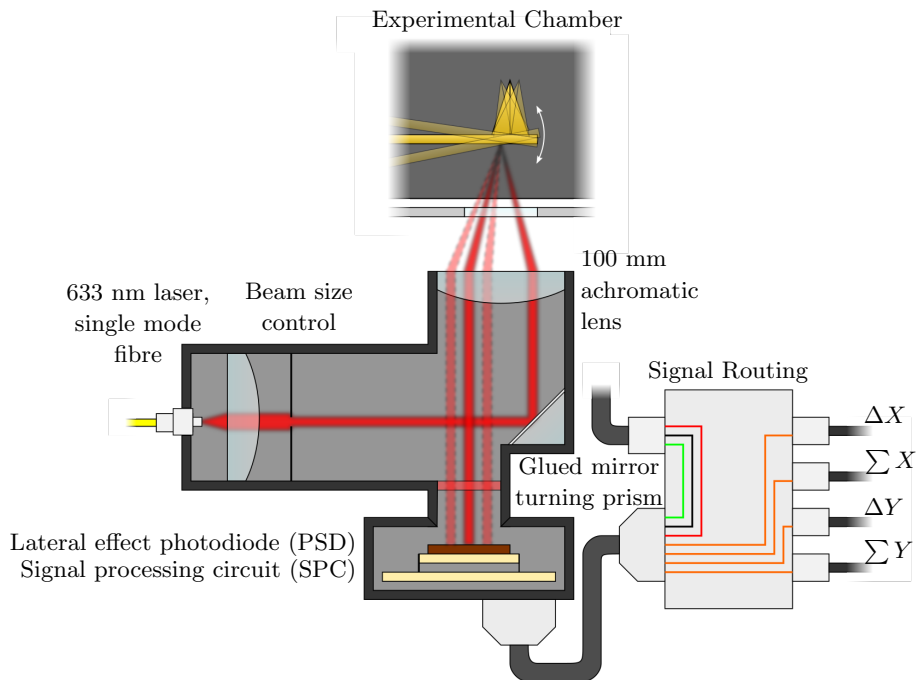


Figure 1.14: Schematic diagram of the AFM module attached to the side of the microscope platform. Incident light from a single mode fibre is focussed at an angle onto an AFM cantilever. Angled reflections from the cantilever are re-collimated into a laterally displaced beam whose position is detected on the PSD.

where i is the lateral axis, either x or y .

1.4.1 Calibrating the AFM

The displacement of the tip under an applied force can be related to the translation of the beam as a measured voltage. By determining the displacement the force applied to the AFM tip can be measured using (1.7). The transformation from displacement into a measured voltage signal can be expressed as,

$$V = k_{x \rightarrow V} x, \quad (1.10)$$

where $k_{x \rightarrow V}$ is the transformation. In the current geometry this transformation is linear and therefore $k_{x \rightarrow V}$ is a fixed constant $k_{x \rightarrow V}$ for a given AFM beam alignment. In general $k_{x \rightarrow V}$ includes each of the transformations required to convert the cantilever displacement into a measurable signal. These transformations are apparent when following the path of the laser beam through the AFM module. The displacement needs to be converted into an angular cantilever deflection, which is further transformed into a translation of the beam after the lens-induced Fourier transform. At this point the displacement requires converting into a current on the PSD and then to the measured voltage after amplification by the 10^5 gain

transimpedance amplifier in the signal processing circuit. Each of these is a linear operation hence the overall effect can be expressed in a single constant $k_{x \rightarrow V}$, which can be experimentally determined.

The simplest method of calibration involves pushing an AFM tip against a hard contact so that the displacement is known ($\Delta z = z$). From there the voltage is measured as a function of displacement and data can be fitted to determine $k_{x \rightarrow V}$. The force can then be estimated using (1.7). Whilst this is not ideal as the cantilever spring constant is still somewhat unknown, the method is simple. Therefore, for force measurements, the value of the cantilever spring constant k from the AFM probe data sheet is assumed. The large tolerances on stiffness measurements are not ideal and mean that this approach is only sufficient to estimate the applied force on a nano-gap to within **less than an order of magnitude**. Other methods of accurately measuring the cantilever spring constant do exist, as do methods to directly map the force to a measured signal, i.e., $F = k_{V \rightarrow F} V$ [], but add further **complexity/complications/requirements** to experiments. Since exact measurements of force are not crucial to current nano-gap studies, less than an order of magnitude is an acceptable uncertainty.

1.5 Scanning Capacitive AFM Tip Alignment

A significant challenge when attempting to recreate a plasmonic dimer using opposing AFM probes is the alignment of probes with the optical (laser) sampling spot in a symmetric tip-to-tip configuration. The ability to align two tips into a dimer configuration is necessary to enable the majority of dual tip experiments. This is the first step when measuring the dynamical physical response of such prototypical dimer systems. For successful experiments the tolerance on the tip-to-tip alignment is less than $\mathcal{O}(R_{tip})$. Aligning tips using CCD imaging in the microscope is limited by diffraction to around **250 nm**. Initially this problem was solved using a non-linear capacitive alignment technique requiring locking into the third harmonic of the driving signal [2]. Whilst functional in simpler systems, the technique was limited in its accuracy due to small ($\mathcal{O}(\text{pA})$) detectable currents in the third harmonic mode and the extensive filtering and lock-in techniques required to measure these. A simpler approach is to simply use the AFM module optics to measure the oscillating cantilever deflection. This is more widely known as scanning capacitance mode AFM (SC-AFM) or scanning capacitance microscopy (SCM). By utilising optical detection over direct electronic measurements tip alignment becomes segregated from the microscope electronic d.c. measurement circuitry and issues are no longer caused by noise leaking into the a.c. electronics.

SCM is a form of AFM used moreso in semiconductor doping analysis than in any other field [3].

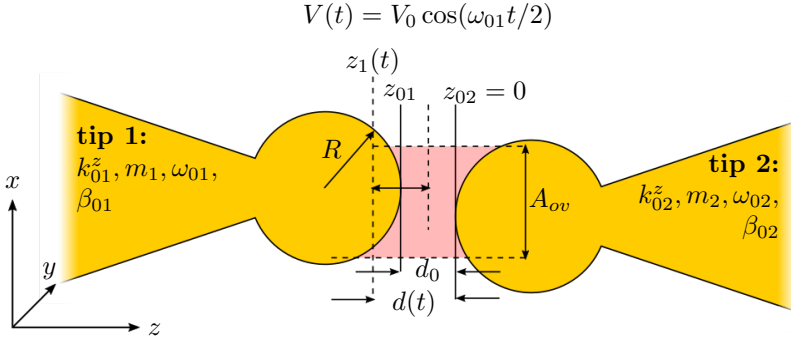


Figure 1.15: Diagram of tip alignment parameters. The position of one tip relative to the other is detected using a resonant scanning capacitance AFM technique. The gap is biased with an oscillating voltage to induce a resonant vibration of one of the AFM cantilevers. The amplitude of oscillation is sensitive to the gap size d and the area of overlap A_{ov} between tip features of characteristic size R . For sharp tips R is the apex radius whereas for nanostructured tips R is considered to be the feature size.

1.5.1 Mechanism for Alignment of Two Opposing Tips

To a first approximation the metallic tips can be ignored and only the capacitive interaction between planar cantilevers is considered. Cantilevers are separated by a distance $d(t) = z_1(t) - z_2(t)$ and coupled via the z -components of the long range attractive electrostatic driving force F_{EL}^z and short range ($\mathcal{O}(\text{nm})$) Van der Waals and repulsive tip-tip interaction forces F_{TT}^z . Each cantilever has an associated spring constant k_{0i}^z , mass m_i and resonant frequency of oscillation $\omega_{0i} = \sqrt{k_{0i}/m_i}$. When vibrated, cantilevers oscillate around an equilibrium position z_{0i} . The equilibrium separation between tips is then denoted by $d_0 = z_{01} - z_{02}$.

The equation describing motion in the z -axis of the two parallel cantilevers, denoted by $i = 1, 2$, of spring constant $k_i^z = k_{0i}^z + k_{TT}^z$, coefficient of damping $\beta_i^z = \beta_{0i}^z + \beta_{TT}^z$ and mass m_i , is given by,

$$m_i \frac{d^2 z_i}{dt^2} + \beta_i^z \frac{dz_i}{dt} + k_i^z (z_i - z_{0i}) = \pm (F_{EL}^z + F_{TT}^z), \quad (1.11)$$

where the sign of the force depends on the tip - positive for one tip and negative for the other. Assuming that alignment takes place at long range, tip-tip interactions can be ignored and $F_{TT}^z = 0$ and therefore $\beta_{TT}^z = k_{TT}^z = 0$. The system is further simplified by assuming that one cantilever remains stationary by being stiff (tapping mode $k \approx 40 \text{ N/m}$) and always being off resonance ($\omega_{01} \neq \omega_{02}$). This is usually satisfied in experiments where a stiff cantilever is required such that the optical probe is incident on the same sample area whilst under force. The apex separation is then restricted to $d = z_1$ with an equilibrium separation $d_0 = z_{01}$. Under these conditions the motion reduces to that of a single tip,

$$m_1 \frac{d^2 z_1}{dt^2} + \beta_1^z \frac{dz_1}{dt} + k_1^z (z_1 - d_0) = F_{EL}^z(z_1, t). \quad (1.12)$$

This equation now describes the whole system rather than each individual tip with the main reference point between tips being the equilibrium separation d_0 .

The remaining capacitive driving force exerted between tips is purely electrostatic and of the form,

$$F_{EL}^z(V, z) = \frac{1}{2} \frac{\partial C(z)}{\partial z} V^2(t), \quad (1.13)$$

where $C(z)$ is the capacitance between the tips at a distance z and $V(t)$ is the potential difference between tips. Under a parallel plate capacitor model the capacitance is $C(z) = \epsilon_0 A_{ov}/z + C_{bk}$ for plates with A_{ov} area of overlap at a separation z , including a stray capacitance C_{bk} . Applying a harmonic driving force at a frequency ω_s , $V(t) = V_0 \cos(\omega_s t)$, results in a nonlinear driving force, given by,

$$F_{EL}^z(z_1, t) = \left(\frac{-\epsilon_0 A_{ov} V_0^2}{4z_1^2} \right) [1 + \cos(\omega_p t)], \quad (1.14)$$

where $\omega_p = 2\omega_s$ is the cantilever pump frequency. Substituting (1.14) into (1.12) gives the simplified equation of motion for the dual-tip system,

$$m_1 \frac{d^2 z_1}{dt^2} + \beta_{01}^z \frac{dz_1}{dt} + k_{01}^z (z_1 - d_0) = \left(\frac{-\epsilon_0 A_{ov} V_0^2}{4z_1^2} \right) [1 + \cos(\omega_p t)]. \quad (1.15)$$

Driving at a pump frequency close to the cantilever resonance ($\omega_p \approx \omega_{01}$) therefore leads to strong resonant oscillations between tips. For small oscillations around d_0 (1.15) can be solved approximately with a solution,

$$z_1 \approx d_0 - |z_1^{off}| - z_{m1} \cos(\omega_p t + \varphi_1) \quad (1.16)$$

where

$$z_1^{off} \approx \frac{\epsilon_0 A_{ov} V_0^2}{4d_0^2 \langle k_{e1}^z \rangle}, \quad (1.17a)$$

$$z_{m1} \approx \frac{\epsilon_0 A_{ov} V_0^2}{4d_0^2 \sqrt{(\langle k_{e1}^z \rangle - m_1 \omega_p^2)^2 + (\beta_{01}^z \omega_p)^2}}, \quad (1.17b)$$

$$\varphi_1 \approx \tan^{-1} \left(\frac{\beta_{01}^z \omega_p}{\langle k_{e1}^z \rangle - m_1 \omega_p^2} \right), \quad (1.17c)$$

in which $\langle k_{e1}^z \rangle$ is the effective spring constant of the system.

Although the model is for two parallel plates, it becomes applicable to tips in a dimer configuration once the separation is sufficiently low that the tip-to-tip capacitance dominates over all other capacitive contributions (such as the cantilever or tip facet interactions). Both the amplitude of the oscillations and the phase, given by (1.17a) and (1.17c), depend on the

tip-to-tip separation d_0 . If the tips stray out of alignment the tip-to-tip distance increases and the capacitance, and by extension the tip oscillation, decreases, hence tips are aligned when the amplitude is maximised. Both properties sensitive to tip alignment can be readily measured using AFM cantilever deflection optics.

Whilst optical detection gives a better signal-to-noise and measures at higher bandwidths, it should be noted that the model was originally developed to show that the $3\omega_s$ current signal can be used to align tips [2]. By driving the system with $\omega_p \approx \omega_{01}$, a mechanical parametric resonance is excited at $2\omega_{01}$ (otherwise only the fundamental is excited with resonant driving) and the current through the tip junction is given by,

$$I(\omega_s) \approx \omega_s C_0 V_0 \left(1 + \frac{|z_{off}|}{d_0} + \frac{z_{m1}}{2d_0} e^{i\varphi_1} + \frac{C_{bk}}{C_0} \right) e^{i\frac{\pi}{2}}, \quad (1.18a)$$

$$I(\omega_p + \omega_s) \approx \frac{(\omega_p + \omega_s) C_0 V_0 z_{m1}}{2d_0} e^{i(\varphi_1 + \frac{\pi}{2})}, \quad (1.18b)$$

where $C_0 = \epsilon_0 A^{ov}/d_0$ and z_{off} is an additional offset due to $F_{EL}^z \propto V^2$. Non-linear oscillations in the tip capacitance result in parametric frequency mixing in the electronics with resulting signals at the sum and difference frequencies, $\omega_p + \omega_s = 3\omega_s$ and $\omega_p - \omega_s = \omega_s$ respectively. The signal at $3\omega_s$ is background-free, as shown in (1.18b), and once again depends only on z_{m1} and d_0 . However, current are small ($\mathcal{O}(\text{pA})$), therefore only alignment works over shorter ranges and requires larger voltages (for larger oscillation amplitudes) and low-noise detection electronics. Optical detection is advantageous as small oscillations at lower voltages are easily detectable, which protects the samples from damage caused by tip tapping when the gap is small.

1.5.2 Numerical Solutions for Tip Alignment

Theoretical curves for the system response based on (1.15) for a typically used contact/tapping mode AFM probe dimer are solved numerically using a ODE solver ⁹. Results are intended to *qualitatively* demonstrate the alignment technique. The following table summarises the parameters of the model for each tip:

	Tip 1	Tip 2
k_0 (N/m)	0.2	40
ω_0 (kHz)	$2\pi.13$	$2\pi.300$
$\Delta\omega$ (Hz)	$2\pi.200$	$2\pi.200$
r (nm)	20	20

The plate area is assumed to be πr^2 where r is the radius of the tip. This is estimated to be $r = 20 \text{ nm}$ based upon standard tip apex dimensions. Changing this value does not

⁹ODE in Numpy/Python.

change the overall qualitative shape of the data. The mass of each tip is calculated from the resonance using $m_i = k_{0i}/\omega_{0i}^2$. The damping coefficient of each tip is given by $\beta_{0i} = 2m\delta_i$ where $\delta_i = \omega_{0i}/2Q_i$ and $Q_i = \omega_{0i}/\Delta\omega$. Only the damping coefficient of the vibrating tip matters at any given time due to the large difference in resonant frequencies. To maximise the detected response the system is studied around the resonance of the soft cantilever. The system spring constant is given by,

$$k_0 = (k_{01}^{-1} + k_{02}^{-1})^{-1}, \quad (1.19)$$

and the system mass is given similarly by,

$$m = (m_1^{-1} + m_2^{-1})^{-1}. \quad (1.20)$$

The damping coefficient of the system is calculated using,

$$\beta = 2m_1\delta_1 \left(1 + \frac{r_1^2}{z} + \frac{(20e^{-6})^2}{z(2 - 20e^{-6})} \right), \quad (1.21)$$

where $\delta = \Delta\omega/2$.

The forces acting on the tip are described by a capacitive driving force, described by (1.14), and an interaction force. The interaction force is described by,

$$F_i^z(z) = \begin{cases} -\frac{Hr_1}{6(a+z_c)^2}, & \text{if } z_c + a > a_0 \\ -\frac{Hr_1}{6a_0^2} + \frac{4E\sqrt{r_1}}{3-3v^2}(a_0 - a - z_c)^{\frac{3}{2}}, & \text{otherwise} \end{cases} \quad (1.22)$$

where z_c is the equilibrium position, a is the amplitude of the oscillation, a_0 is the equilibrium separation and H is the Hamaker constant. The capacitive driving force depends only upon the time-averaged tip separation whereas the interaction force depends on if the amplitude of the tip from its equilibrium separation causes contact/tapping with the other tip.

The ODE solving algorithm computes the change in the cantilever position and velocity in time using their respective differentials,

$$\dot{z}_+ = \dot{z}_-, \quad (1.23)$$

$$\ddot{z} = -m^{-1} [\beta_1^z \dot{z} - k_0^z z + F_{EL}^z(t) + F_i^z(z)], \quad (1.24)$$

where $F_{EL}^z(t)$ is the capacitive driving force described in (1.14), $F_i^z(z)$ is the interaction. The response of the system in time to an applied force, subject to initial conditions, is solved for 100 AFM oscillation periods. The steady state harmonic properties of the waveform are then extracted using a sinusoidal fit to the last 50 periods. After 50 periods the system response has reached its steady state and is in most cases stable.

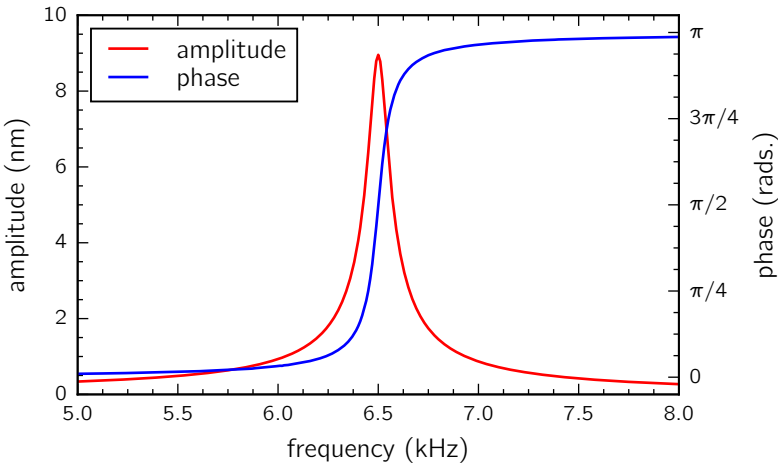


Figure 1.16: Theoretical frequency response showing the amplitude and phase of a 13 kHz-300 kHz opposing AFM tip system. The tip junction is held at 10 V with a 100 nm intertip separation.

By driving a spatially fixed dimer system (tips separated by 100 nm and biased with 10 V) around $\omega_s = \omega_{01}/2 = 2\pi \cdot 13 \text{ kHz}/2$ the frequency response of the tip dimer is determined and the tip resonance can be clearly seen. The intertip separation is then reduced while maintaining the resonant driving signal at $\omega_{01}/2$ to find the separation response. Figure 1.16 shows the frequency response scanning through resonance. The line follows a Lorentzian line shape, typical of damped resonators, with a π phase change when passing through resonance. The tip oscillates in phase with the second harmonic driving force below resonance and passes into anti-phase above resonance, in accordance with most resonators [1].

The separation response is shown in Figure 1.17. As the separation decreases the capacitance between tips increases and the oscillation is amplified. This amplification occurs until the oscillation amplitude is equal to the separation, at which point the system transitions into the more regularly used tapping mode of AFM imaging. This is shown by the linear relationship between amplitude and separation regardless of voltage. In this regime the oscillation is restricted by the gap width between tips and so the separation limits the maximum possible amplitude. Phase contrast only occurs once the oscillating tip can come into close proximity with the other tip. This degree of separation is confirmed by the onset of phase contrast being close to the point of maximum amplitude. The phase is therefore a good indicator of alignment between tips. Tips can be considered to be aligned once the amplitude and phase centres agree. The accuracy of these solutions becomes limited when the separation is reduced well into the tapping mode regime as the oscillation is difficult to sustain and surface (interfacial) forces begin to dominate leading to the snap-to-contact effect. This instability is seen by the deviation of the amplitude from its linear decrease in the tapping regime followed by its rapid decay.

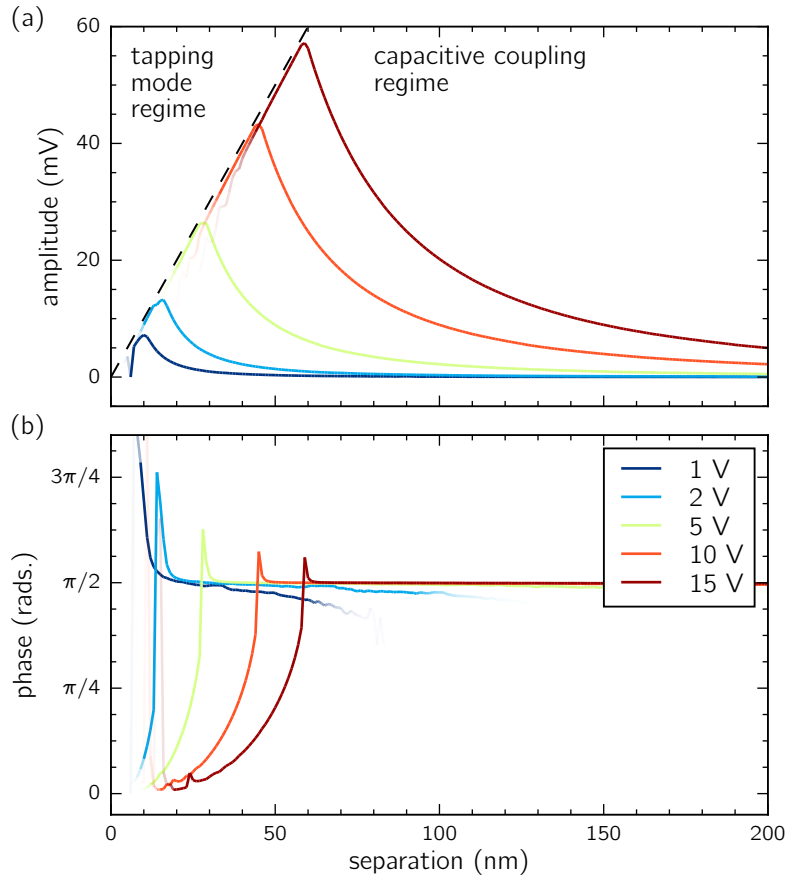


Figure 1.17: Theoretical separation response showing the amplitude (a) and phase (b) of a 13 kHz-300 kHz opposing AFM tip system. The voltage across the tip junction is varied while on resonance ($\omega_s = 2\pi \cdot 6.5$ kHz). The amplitude increases as the intertip separation is reduced. The dashed line shows the point at which the oscillation amplitude is equal to the separation. For separations below this limit the hard surface restricts the amplitude to the gap between tips.

1.5.3 Experimental Measurements using Scanning Capacitance Microscopy

Experimental measurements of capacitive tapping mode tip interaction use the AFM optics on the microscope. The backside of the softer cantilever of the pair is illuminated by the 633 nm laser beam from the AFM module. Reflected light from the cantilever is directed onto the position sensitive detector (PSD) where it generates a current depending on the location of the laser spot on the sensor. By resonantly driving an AFM tip electronically its oscillation generates a signal $A \cos(\omega_p t + \phi)$ along one of the axes on the PSD. The current from the PSD is converted into an amplified voltage after padding through a signal processing circuit and transimpedance amplifier (10^5 gain). Lock-in detection is used to remove noise and add phase sensitivity to signal measurements by referencing the oscillation to the driving signal. Since the oscillation signal is large lock-in detection is performed using software rather than hardware, increasing the simplicity and reducing the overall cost of the setup. The NIDAQ

device simultaneously acquires both the AFM PSD signals in each direction and the driving signal from the function generator output. The software lock-in detects the amplitude and phase of the tip oscillation by locking in on and isolating the second harmonic driving frequency ω_p using the reference periodicity. The phase difference ϕ is therefore measured between the signal and the reference.¹⁰

The resonance frequency of the (**softer**) **back-facing** cantilever is determined prior to alignment by scanning the driving signal frequency and measuring the cantilever response. By mapping the lateral amplitude and phase variations of the cantilever deflection on resonance two opposing tips can be experimentally aligned. The location of the opposite tip is determined from the centroid of the mapped amplitude and phase variations. This procedure is advantageous as it operates at long range in the non-contact regime, prior to the tapping mode regime.

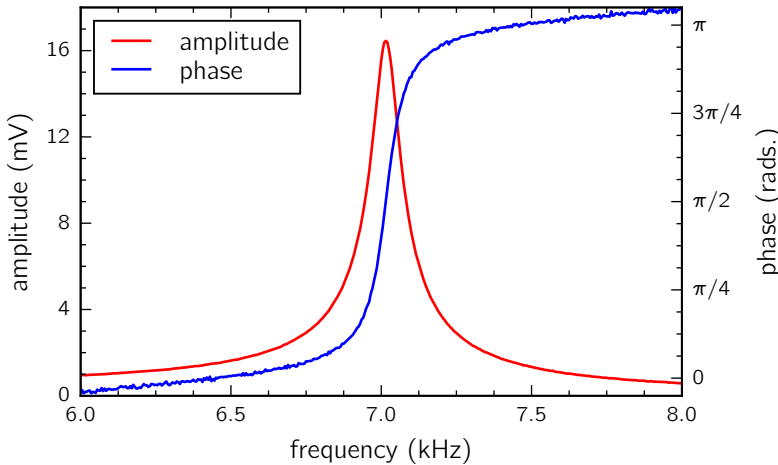


Figure 1.18: Resonance scan of a standard Au contact mode AFM tip opposite a standard Au tapping mode AFM tip. The soft tip (BudgetSensors ContGB) has a 13 kHz resonant frequency and the stationary tip is resonant at 190 kHz (BudgetSensors TapGB). Cantilevers are separated by $\sim 1 \mu\text{m}$ and driven at 10 V.

The measured frequency response of a capacitively-driven AFM cantilever (Figure 1.18) agrees well with the modelled response (Figure 1.16). One difference is the linear gradient superimposed onto the phase response. This stems from time lags during acquisition which give a linear phase offset with increasing frequency.

The separation response is probed by aligning a soft (13 kHz, 0.2 N/m) tip to the maximum amplitude signal by laterally scanning the xy plane opposite a stiff (190 kHz, 48 N/m) tip. The soft tip is then approached towards the stationary tip along the z axis in $\mathcal{O}(\text{nm})$ steps and the cantilever response is measured. The amplitude is monitored in real time and the tip is retracted once the signatures of tapping are detected and the regime is deemed to be unstable to effects such as snap-in and short-range attractive forces or when there is a chance of damaging

¹⁰The details of the lock-in procedure are detailed in the appendices.

the tip. This judgement is subjective but preserves the tip for multiple cycles. This approach-reaction cycle is repeated many time with a continuously reducing voltage until tapping is difficult to achieve without immediately becoming unstable. This occurs once driving the oscillation with less than 5–6 V.

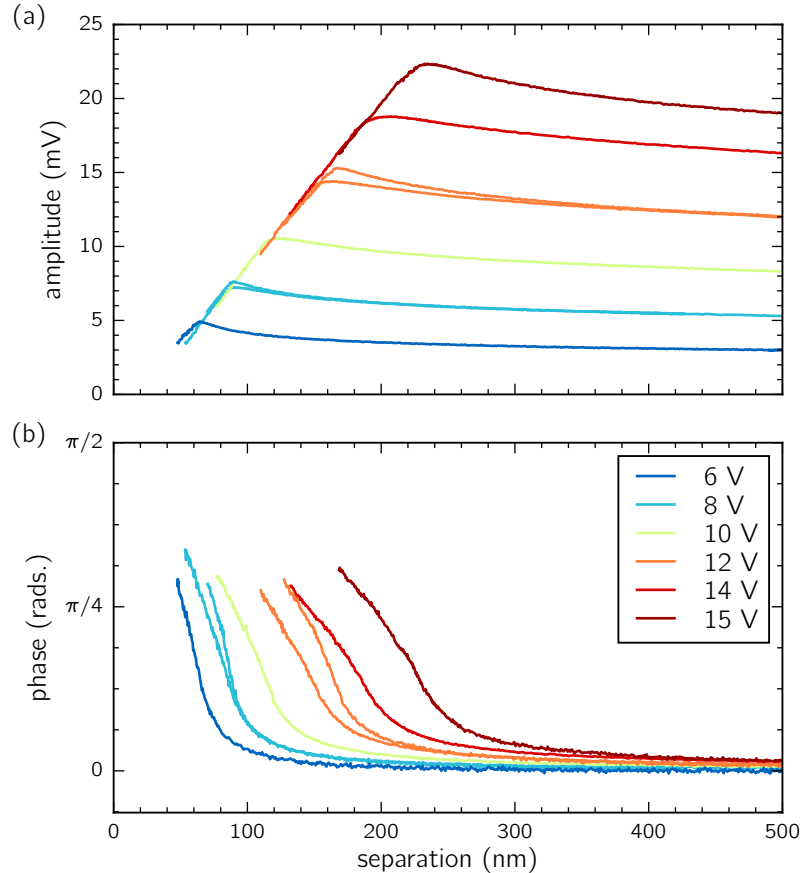


Figure 1.19: Experimental separation response showing the amplitude (a) and phase (b) for a standard Au contact mode AFM tip approaching a standard Au tapping mode AFM tip. The same vibrating tip is approached and retracted with the voltage reduced between each approach cycle. The amplitude increases as the intertip separation is reduced until oscillation becomes restricted by the gap width.

Figure 1.19 shows the corresponding experimental curve to the numerically calculated separation response shown in Figure 1.17. The expected capacitive increase in amplitude followed by a linear tapping mode regime is found in the experimental data. A significant difference from the model is that the baseline capacitive amplitude increase is not as drastic. This is likely due to the large extended shape of the tip. This was not taken account in numerical calculations which use only a simple parallel plate model. The linear decrease is also less steep suggesting that only the upper region of the modelled curve is visible. The amplitude instabilities found in the theory for small separations and large driving amplitudes are also found in the experimental data. Repeat approaches after such an instability show different peak amplitudes with the differences attributed to misalignment after contact, changes in tip

morphology or surface modification. Interestingly the discontinuous reduction in the phase difference is not observed in the experiment. Either this means that a sufficiently restricted amplitude was not reached before retracting or that there is deviation from the simple model. Overall the cantilever behaviour qualitatively matches many of the trends predicted using a simple mathematical model solved using an ODE solver.

Figure 1.19 further demonstrates that this technique has the capability to lock the positions of the tips relative to each other at long range by using the graded separation response as a feedback mechanism. Dynamic positioning and alignment between two tips can then be locked and maintained through an experiment to account for fluctuations due to either mechanical or thermal drift. By using a *pid* feedback loop and selecting a target amplitude the average position can be locked provided that the tip remains oscillating. By decreasing the voltage, oscillation can be reduced but only up until the point at which the second harmonic signal becomes difficult to detect. The onset of tapping also limits the minimum achievable separation though gap sizes well below 100 nm remain possible. This technique could become more useful if a stable plasmonic gap size is required throughout an experiment whilst the contents or properties of the gap are modified.

1.5.4 Experimental Alignment of Tips using Scanning Capacitance AFM

Alignment between tips is carried out on resonance by laterally scanning the oscillating cantilever tip over the stationary, typically stiffer, tip whilst reducing the separation. To prevent tip collisions due to entering the tapping mode regime, the voltage is also reduced along with the separation. This allows only the minimum required signal for positional analysis. Unlike the phase, the amplitude signal varies smoothly over a longer range. By iteratively following the lateral position of maximum amplitude the tips can be brought into alignment. As the intertip separation decreases and the amplitude converges on this value the phase starts to increase forming a distinct, sharp peak around the tip apex.

Figure 1.20 shows a typical alignment scan at close range with peaks in both the amplitude and phase when raster-scanning one tip over the other. At this point during the procedure the tips could be considered to be well aligned.

Since the tips are only symmetric in one direction capacitive coupling is **inhomogeneous and skewed** until the distance between tips is small enough that the tip-to-tip capacitance dominates over the larger scale interactions. Gaussian fitting therefore can be potentially inaccurate in determining the peak location. Calculating the discrete image moments provides a more accurate, and faster, way of centring the scanned tip on the opposing tip. These are

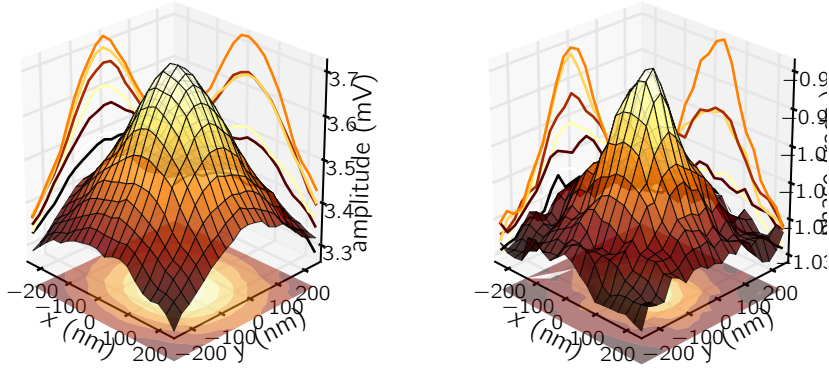


Figure 1.20: Alignment scan of a soft Au AFM tip scanned laterally over a hard Au AFM tip. The soft tip is oscillating at 13 kHz (BudgetSensors ContGB) while the 190 kHz Au tip (BudgetSensors TapGB) remains static. Tips are separated by ~ 50 nm and driven at 8 V. Strong peaks are seen in both the amplitude and the phase of the soft cantilever oscillation. The tips are aligned in a tip-to-tip configuration when both signals are maximised.

calculated using,

$$M_{ij} = \sum_x \sum_y x^i y^j I(x, y), \quad (1.25)$$

where i, j denote the possible axes $[]$.¹¹ The integrated intensity or area of an image is given by the moment $M_{00} = \sum_x \sum_y I(x, y)$. The centroid of the image is then given by,

$$(\bar{x}, \bar{y}) = \left(\frac{M_{10}}{M_{00}}, \frac{M_{01}}{M_{00}} \right). \quad (1.26)$$

By tracking the centroid calculated at the end of each lateral scan whilst decreasing the tip separation from larger distances ($\sim 1 \mu\text{m}$) to separations near to 50 nm tips are brought into alignment.

Alignment is classified as the point at which the amplitude centroid is in agreement with the phase centroid. This criterion for alignment is chosen since the phase centroid does not deviate significantly from the initial position from which it emerges (Figure 1.21(b)), despite only appearing once the separation has become sufficiently small. The amplitude centroid, on the other hand, follows the point of maximum capacitive coupling which depends sensitively on the separation regime and the driving voltage (Figure 1.21(a)). The accuracy of the alignment can be quantified from the FWHM of both the amplitude and phase peaks. The FWHM of both centroids shortly after passing the alignment threshold constrict to a similar length scale as the feature size dictating the short range alignment, such as the radius of a sharp or

¹¹Note that the discrete image moments are based on the continuous moment theorem with moments given by

$$M_{ij} = \int_{-\infty}^{\infty} \int_{-\infty}^{\infty} x^i y^j f(x, y) dx dy.$$

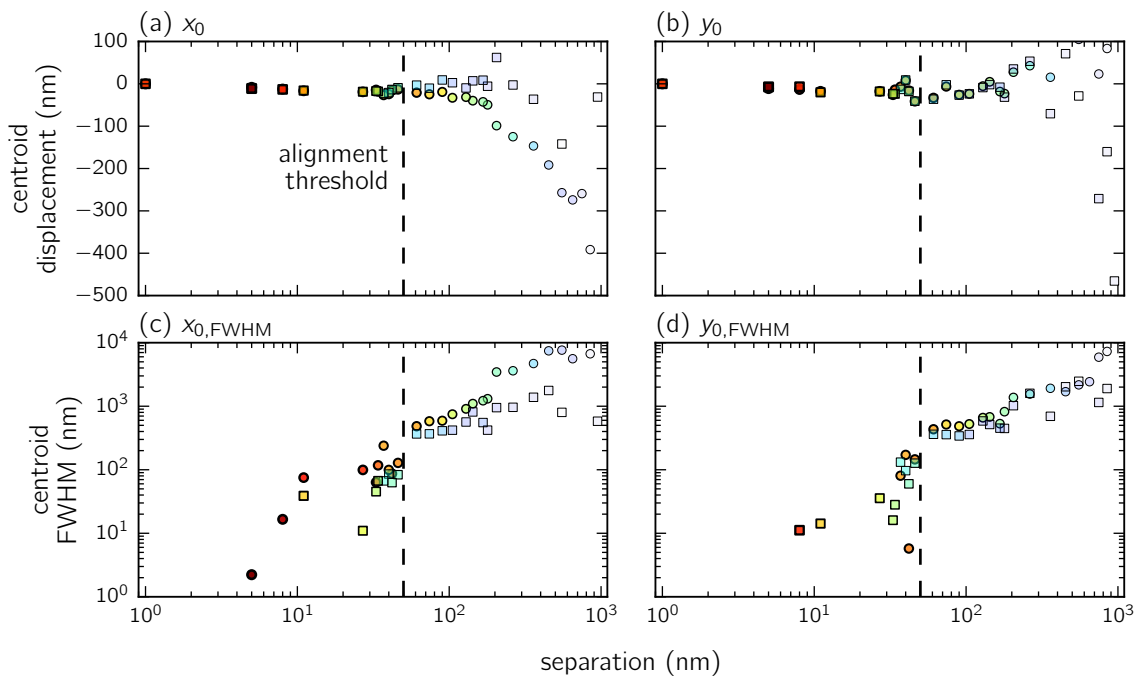


Figure 1.21: Centroid tracking during approach and alignment of two sharp Au tips. Amplitude (circles) and phase (squares) centroid positions relative to final alignment are shown in both the x (a) and y (b) directions. The centroid FWHM for the x and y amplitude and phase centroids are shown in (c) and (d), respectively. The final separation is an order of magnitude estimate based on the tapping mode linearity.

spherical tip apex. This level of localisation is directly visible in the data (Figure 1.21(c,d)) where alignment using sharp Au tips results in a final FWHM between 10–30 nm. When studying spherical tips with 150 nm radii it is noticed that the FWHM remains much larger since the surfaces in close proximity are much flatter in comparison.

The prerequisite requirements of this technique impose limitations as to which tip dimers can be formed. Tips necessarily have to be conductive to generate a strong capacitive signal at the tip junction and induce a cantilever resonance.¹² Due to the increased sensitivity and signal-to-noise when using optical detection compared to electronics for long range alignment this technique is able to align together tips including those with smaller oscillations. This means that for a standard Au tip dimer (one contact, one tapping mode cantilever) alignment is possible at voltages as low as 2 V, the minimum driving voltage of the input amplifier, for small tip separations. This means a lower current and a smaller oscillation amplitude, therefore less chance of damaging tips.

Coupled with the higher bandwidth that the PSD offers (400 kHz) compared with sensitive electronics (100 kHz), this alignment technique has demonstrated the capability of aligning together pairs of cantilevers stiffer than the typically used contact mode probes. Cantilever

¹²However it should be noted that Si tips have been aligned using this technique. Si AFM tips are generally doped to dissipate static charge. Here it is found that they are doped sufficiently to give an adequate capacitive response.

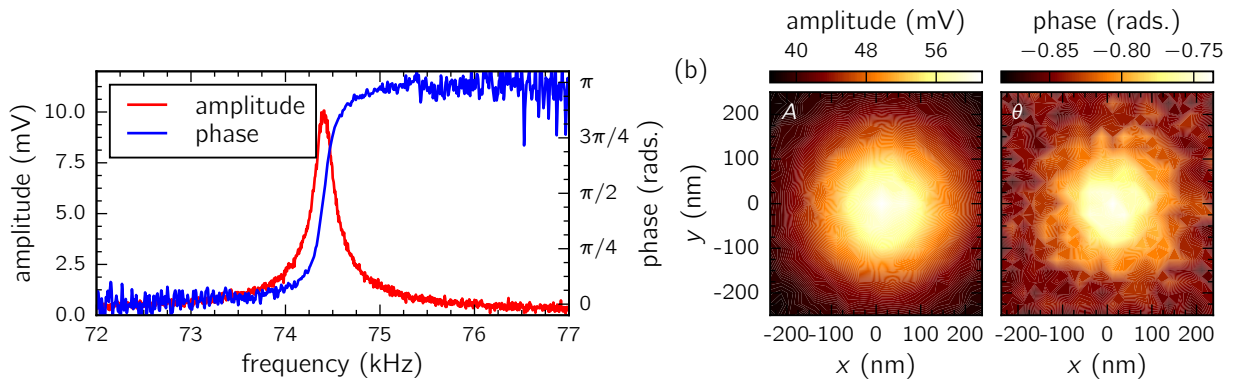


Figure 1.22: High frequency alignment data for a tip dimer composed of two 48 N/m Au AFM tips. Tips are separated by ~ 50 nm and driven at 120 V. (a) Frequency response of the system. (b) Amplitude and phase alignment scans.

resonances have been detected and alignment successfully performed for tip dimers comprised of $k = 48$ N/m tapping mode (190 kHz) AFM probes (Figure 1.22), though in these cases the necessary driving voltage is increased to around 100 V.

To summarise, the capacitive alignment technique developed by Savage *et al.* [2] has been successfully adapted to use optical cantilever detection, as in AFM, instead of direct electronic measurements of the tip junction. The technique is greatly improved, is less sensitive to other electronic systems integrated into the microscope, and has demonstrated the capability to align two tips to within 10 nm of the target - less than the feature size of the tips. Both the frequency and spatial response is studied to show the tip separation dependence and the resulting alignment mechanism.

1.6 Conclusions

A custom-built ultra-stable microscope platform, utilising supercontinuum dark-field spectroscopy, low-noise electronics and atomic force microscopy, is built to accommodate spectral studies of both individual tips and tip dimers. The platform is capable of taking two tips and aligning them into a dimer configuration using a modified form of scanning capacitance microscopy. Performance characterisation shows spectral validity between 500–1100 nm, more broadband than standard optical microscopes, with confocal localisation enabling the study of more complex structures than point scatterers.

References

- [1] “Crc handbook of chemistry and physics”, in, edited by W. M. Haynes (CRC press, 2013).
- [2] K. J. Savage et al., “From microns to kissing contact: dynamic positioning of two nano-systems”, *Applied Physics Letters* **99**, 053110 (2011).
- [3] Y Huang, C. Williams, and J Slinkman, “Quantitative two-dimensional dopant profile measurement and inverse modeling by scanning capacitance microscopy”, *Applied physics letters* **66**, 344–346 (1995).